M. Dile, K. Laganovska, A. Zolotarjovs, I. Bite, E. Vanags, I. Pudza, A. Kuzmin, K. Smits,
The effect of surfactants and precursors on the structure and properties of ZnS:Cu nanocrystalline particles,
Nano-Struct. Nano-Objects 35 (2023) 101023. Doi: 10.1016/j.nanoso.2023.101023.

The effect of surfactants and precursors on the structure and properties of ZnS:Cu nanocrystalline particles

Milena Dile, Katrina Laganovska*, Aleksejs Zolotarjovs, Ivita Bite, Edgars Vanags, Inga Pudza, Alexei Kuzmin, Krisjanis Smits

Institute of Solid State Physics, University of Latvia, Kengaraga Str. 8, Riga, LV-1063, Latvia

* Corresponding author: E-mail address: katrina.laganovska@cfi.lu.lv (K. Laganovska).

Doped ZnS materials exhibit excellent optical and electrical properties, making them a superior material for alternating current (AC) thin film electroluminescent devices, solar panels, light-emitting diodes, laser diodes and other luminescent device designs and fabrications. This study involves the hydrothermal synthesis of nanocrystalline Cu-doped ZnS materials without a surfactant and using two surfactants – hexadecyltrimethylammonium bromide (HTAB) and sodium dodecyl sulfate (SDS). The structure, morphology and elemental content of the synthesized nanopowders were characterized by X-ray powder diffraction, X-ray absorption spectroscopy (XAS), scanning electron microscopy and energy-dispersive X-ray spectroscopy (EDX) techniques, while the optical properties were studied by photoluminescence (PL) spectroscopy. The sizes of the nanocrystallites in all the synthesized samples were below 20 nm. XAS results suggest that Cu ions substitute Zn ions in cubic zinc blende ZnS structure and are located in a locally distorted environment. The addition of a surfactant allows control of the morphology of the particles and their photoluminescent properties.

Keywords: ZnS:Cu, X-ray absorption spectroscopy, Photoluminescence, Hydrothermal synthesis, Surfactants

1. Introduction

Over the past several years, the photoluminescent, electroluminescent and catalytic properties of type II-VI crystalline semiconductors have been extensively studied. One of the most common materials is the low-cost, non-toxic and environmentally friendly zinc sulfide (ZnS) [1]. Its properties change significantly when transition metal ions are incorporated into the host crystal lattice. The optical and electrical properties of zinc sulfide materials doped with other elements make it an important material for the production of devices such as alternating current thin film electroluminescent (ACTFEL) devices, solar cells [1], flat screens and displays, laser diodes or light-emitting diode lamps [2], and in chemo/biosensing applications [3].

New methods of synthesis are still being developed for doped ZnS materials in order to obtain optimal structure, morphology and optical properties. An effective and environmentally friendly nanomaterial synthesis method is the hydrothermal method. It is based on the fact that water and aqueous solutions can dis- solve highly insoluble materials at high temperatures under high pressure [4]. This technique could be used for ACTFEL device production as a transparent light-emitting layer, as well as increasing the number of available visible light emission colors. The improvement of the transparency of ACTFEL panels still remains a significant challenge [5].

Many studies report that ZnS crystalline phase composition, crystallite size and distribution have a great influence on the transparency of a material [6–10]. Bulk ZnS crystallizes in two phases – the cubic phase (zinc blende or sphalerite), which is stable at room temperature and normal pressure, and a metastable hexagonal (wurtzite) phase, existing at temperatures above 1020 °C [11]. Many studies show that the ZnS hexagonal phase exhibits photoluminescence with greater intensity than the cubic phase [12]. However, Chen et al. have demonstrated that the hexagonal phase decreases the optical transparency by causing birefringence [7].

In this study, we outline the synthesis of ZnS:Cu using a surfactant-assisted hydrothermal method. The effect of different surfactants on the particle structure, morphology, agglomeration and elemental composition was identified using X-ray diffraction (XRD), X-ray absorption spectroscopy (XAS), scanning electron microscopy (SEM) and energy-dispersive spectroscopy (EDX). Additionally, the optical properties were studied by photoluminescence spectroscopy (PL).

2. Materials and methods

2.1. Materials

Zinc chloride ($ZnCl_2$, purity 99.9%; Supelco), zinc acetate dihydrate ($Zn(CH_3COO)_2 \cdot 2H_2O$, purity 99.5%; Alfa Aesar), sodium

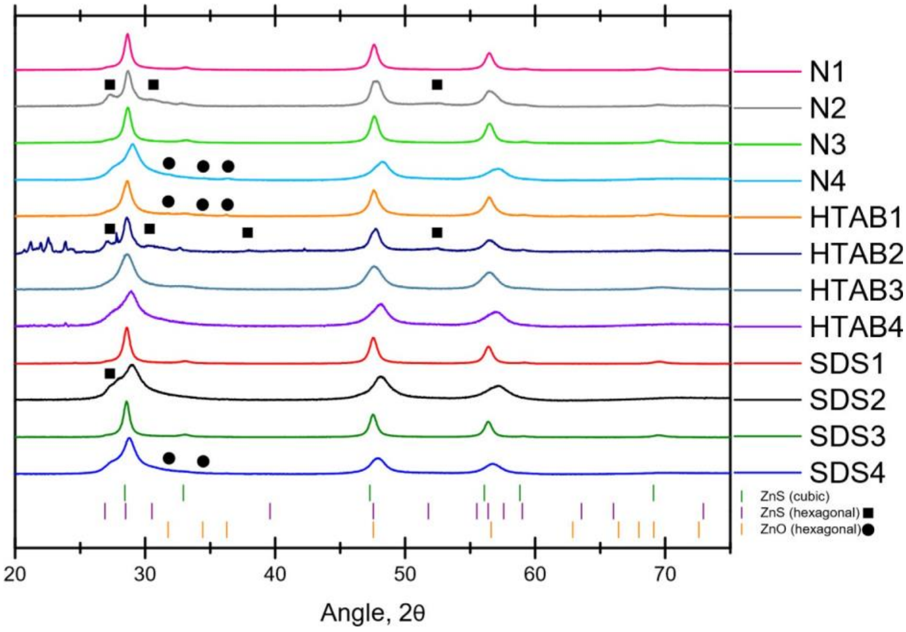

Fig. 1. X-ray diffraction patterns of the hydrothermally synthesized ZnS:Cu powders.

sulfide ($NaS_2 \cdot 9H_2O$, purity 98%; Acros Organics) and thiourea ($CS(NH_2)_2$, purity 99.9%; Carl Roth GmbH + Co. KG) were used as the main precursors for the ZnS synthesis. Copper(II) sulfate pentahydrate ($CuSO_4\ 5H_2O$, purity 97%; Sigma Aldrich) was used as a dopant source. The reaction was carried out in deionized (DI) water (H_2O, 99.5%; electroconductivity 18.2 MΩ/cm at 25 °C; TOC (Total Organic Carbon) < 20 ppb; microorganisms < 10 CFU/ml; heavy metals < 0.01 ppm; silicates < 0.01 ppm; total solids content < 0.03 ppm) media. Hexadecytrimethylammonium bromide (HTAB, purity 99.9%; Merck) and sodium dodecyl sulfate (SDS, purity 98%; Fluka) were used as surfactants. Ethanol (C_2H_5OH, purity 96%; Supelco) was used for the storage of the synthesis product as a suspension. All the chemicals were used without any further purification.

2.2. *Synthesis*

1.5 at.% Cu-doped ZnS materials were synthesized by the hydrothermal method (Table 1). First, two solutions (A and B) were prepared separately at room temperature under constant stirring. Solution A was prepared by dissolving $ZnCl_2$ or $Zn(CH_3COO)_2\ 2H_2O$ (0.197 M) in 45 mL DI water. After 15 min, 0.2 mmol of $CuSO_4\ 5H_2O$ (0.003 M) was added. 15 min after the complete dissolution of metal salts, the surfactant HTAB (0.01 M) or SDS (0.01 M) was added to the solution. Solution B was prepared by dissolving $NaS_2 . 9H_2O$ or $CS(NH_2)_2$ (0.17 M) in 45 mL DI water. Both solutions were stirred at room temperature with a constant speed for 45 min to obtain a transparent homogeneous solution. Then, solution A was poured into the Teflon-lined stainless-steel autoclave, after which solution B was dropwise added to the mixture (without stirring), and the autoclave was tightly sealed. Subsequently, the hydrothermal reaction was carried out at 160 °C temperature for 22 h with a heating rate 5 °C min^{-1} in a laboratory heating-drying oven Nabertherm TR 60. After the hydrothermal reaction, the mixture was naturally cooled down and a greyish-green sol was obtained. The ZnS materials were separated from the solvent by centrifugation and purified by washing them 6 times with 15 mL DI water for 30 min at 9000 rpm.

Table 1
Reagents used for hydrothermal synthesis.

Sample	Zinc precursor	Sulfur precursor	Surfactant
N1	$ZnCl_2$	$Na_2S \cdot 9H_2O$	–
HTAB1	$ZnCl_2$	$Na_2S \cdot 9H_2O$	HTAB
SDS1	$ZnCl_2$	$Na_2S \cdot 9H_2O$	SDS
N2	$ZnCl_2$	$CS(NH_2)_2$	–
HTAB2	$ZnCl_2$	$CS(NH_2)_2$	HTAB
SDS2	$ZnCl_2$	$CS(NH_2)_2$	SDS
N3	$Zn(CH_3COO)_2 \cdot 2H_2O$	$Na_2S \cdot 9H_2O$	–
HTAB3	$Zn(CH_3COO)_2 \cdot 2H_2O$	$Na_2S \cdot 9H_2O$	HTAB
SDS3	$Zn(CH_3COO)_2 \cdot 2H_2O$	$Na_2S \cdot 9H_2O$	SDS
N4	$Zn(CH_3COO)_2 \cdot 2H_2O$	$CS(NH_2)_2$	–
HTAB4	$Zn(CH_3COO)_2 \cdot 2H_2O$	$CS(NH_2)_2$	HTAB
SDS4	$Zn(CH_3COO)_2 \cdot 2H_2O$	$CS(NH_2)_2$	SDS

2.3. *Characterization*

The structure of undoped and Cu-doped ZnS powders was determined by the X-ray powder diffraction (XRD) technique. The XRD patterns (Fig. 1) were recorded using a benchtop Rigaku MiniFlex 600 diffractometer with the Bragg–Brentano θ -2θ geometry equipped with a 600 W X-ray tube (Cu Kα radiation), operated at 40 kV and 15 mA. The lattice parameters (a) and crystallite sizes (D) were calculated from the XRD patterns based on the Rietveld refinement method (Table 2), performed using the Profex code [13].

A scanning electron microscope (SEM), Thermo Fisher Scientific Phenom Pro operated at 10 kV voltage, was used to examine the morphology of all the samples in the full backscattered (BS) mode. A SEM Thermo Fisher Scientific Helios 5 UX was used for extra examination of samples N1, N3, HTAB1, HTAB3, SDS1 and SDS3 in the secondary electron (SE) mode. The elemental composition of all the samples was studied by the same SEM using energy dispersive X-ray spectroscopy (EDX). The SEM was operated at 2 kV voltage for imaging and during the elemental analysis at 30 kV. Additionally, a focused ion beam (FIB) was used for dissection of the nanoparticles.

Photoluminescence (PL) measurements were performed at room temperature using a YAG laser FQSS266 (CryLas GmbH)

Table 2
The phase composition (c-cubic, h-hexagonal), lattice parameter *a* (Å), crystallite size *D* (nm) and R-factors obtained by the Rietveld refinement of the XRD patterns.

Sample	Phase	a, Å	D, nm	Rwp, %	Rexp, %
N1	100% (c)	5.408(2)	14.9(2) (c)	10.5	2.5
HTAB1	98.4(2)% (c), 1.6(2)% (ZnO h)	5.405(2)	10.4(2) (c)	8.4	2.6
SDS1	100% (c)	5.410(2)	15.3(2) (c)	13.1	2.5
N2	33.6(7)% (c), 66.4(7)% (h)	5.410(2)	12.5(2) (c), 4.4(2) (h)	7.1	2.3
HTAB2	47.2(2) % (c), 52.8(2)% (h)	5.410(2)	11.2(2) (c), 7.1(2) (h)	12.6	2.2
SDS2	49.8(2)% (c), 50.2(2)% (h)	5.400(2)	5.6(2) (c), 3.4(2) (h)	7.4	2.3
N3	100% (c)	5.409(2)	14.4(2) (c)	10.3	2.5
HTAB3	100% (c)	5.401(2)	6.8(2) (c)	8.1	2.4
SDS3	100% (c)	5.410(2)	16.6(2) (c)	10.7	2.6
N4	98.4(2)% (c), 1.6(2)% (ZnO h)	5.400(2)	4.8(2) (c)	12.6	2.3
HTAB4	100% (c)	5.400(2)	4.6(2) (c)	9.1	2.4
SDS4	99.1(2)% (c), 0.89(2)% (ZnO h)	5.400(2)	5.6(2) (c)	14.0	2.2

4th harmonic at 266 nm (4.66 eV). All samples were pressed into pellets of equal size, which made it possible to compare the PL intensity between the samples. The PL spectra were recorded using an Andor Shamrock B-303i spectrograph equipped with a CCD camera (Andor DU-401A-BV).

X-ray absorption spectroscopy was used to probe the local environment around the Zn and Cu ions in the Cu-doped ZnS powders. The experiments were performed in transmission (at the Zn K-edge) and fluorescence (at the Cu K-edge) modes at the DESY PETRA-III P65 Applied XAFS beamline [14]. PETRA-III storage ring operated in the 40 bunch top-up mode with an energy of 6 GeV and current of 100 mA. The synchrotron radiation was monochromatized using a fixed-exit double-crystal monochromator Si(111) and the harmonic reduction was achieved using Rh-coated silicon plane mirrors. The X-ray intensity before and after the sample was monitored using two ionization chambers and the X-ray fluorescence was simultaneously measured using a passivated implanted planar silicon (PIPS) detector (Canberra). The samples were prepared as pellets by mixing the ZnS:Cu powder with cellulose and measured in a liquid helium flow cryostat (Janis Research Company, LLC) at 10 K to reduce the effect of thermal vibrations. The sample thickness was optimized to obtain an absorption Zn K-edge jump equal to one. The extended X- ray absorption fine structure (EXAFS) was extracted from the experimental X-ray absorption spectra using the XAESA code [15] following a conventional procedure [16].

2.4. EXAFS data analysis

The reverse Monte Carlo (RMC) method, as implemented in the EvAX code [17,18], was used for the analysis of the EXAFS spectra $\chi(k)k^2$ for the SDS2 and SDS3 samples recorded at the Cu and Zn K-edges. The wavenumber k is defined as $k = k$ $= (2m_e/\hbar^2)(E - E_0)$ where m_e is the electron mass, $\hbar$ is the Planck constant and E_0 is the threshold energy, i.e. the energy of a free electron with zero momentum. The RMC method is based on the evolutionary algorithm (EA), which significantly accelerates the optimization procedure [18] and uses the Morlet wavelet trans- form (WT) for a comparison of the experimental and calculated EXAFS spectra simultaneously in k and R spaces [19]. Such an approach was successfully used by us recently to study the local environment of Zn and Mn ions in Mn-doped ZnS [20].

RMC/EA simulations were performed using the structural model represented by the $4a \times 4a \times 4a$ supercell (simulation box) of the cubic zinc blende lattice [21] with the lattice pa- rameter $a = 5.356$ Å for SDS2 and $a = 5.415$ Å for SDS3, obtained from the Rietveld refinement of the XRD patterns. The simulation box contained 512 atoms: 240 zinc atoms, 16 copper atoms and 256 sulfur atoms. The Cu atoms were placed so that the smallest distance between each two of them was larger than 10 Å, which ensures that the local environment around each of the Cu atoms can relax independently in the RMC simulations. Periodic boundary conditions were used to avoid surface-related effects. The atoms were allowed to displace by up to 0.4 Å from their positions in the ideal zinc blende structure. The number of atomic configurations simultaneously considered in the EA algorithm was 32 [18].

The configuration-averaged (CA) EXAFS spectrum $\chi(k)$ was calculated at each step of the RMC/EA simulation over all the absorbing atoms of the same type (Zn or Cu) located in the simulation box. The EXAFS spectra for each atom were evaluated using ab initio real-space multiple-scattering FEFF8.5L code [22,23], taking into account the multiple-scattering (MS) effects up to the fourth order. The total number of RMC steps was 5000 to guar- antee the convergence of the structural model. The agreement between the Morlet wavelet transforms (WTs) of the experi- mental and CA EXAFS spectra $\chi(k)k^2$ was used as a criterion for the model structure optimization. The WT calculations were performed in the k-space range of 2.8–17.0 Å at the Zn K-edge and 3.0–11.0 Å at the Cu K-edge. The WT calculations in the R- space were done in the range of 1.0–6.0 Å for both absorbing atoms. Both the Zn and Cu K-edge EXAFS spectra were fitted simultaneously using the same structural model.

The final atomic coordinates in the simulation box were used to calculate the radial distribution functions (RDFs), $g(R)$. To improve statistics, ten different (independent) structural models were generated and used for the final RDFs. The mean-square displacements (MSDs) were evaluated for the Zn, S and Cu atoms, and the mean-square relative displacements (MSRDs) were calculated for Zn–S, Zn–Zn, Cu–S and Cu–Zn atom pairs.

3. Results and discussion

3.1. XRD

XRD patterns (Fig. 1) indicate the formation of nanocrystalline compounds with broadened Bragg peaks. The dominant phase in the synthesized samples is the cubic zinc blende phase [21], with the space group $F\bar{4}3m$ (No. 216). However, the sample HTAB2 contains, in addition, an unidentified phase that may be associated with the thermal decomposition products of HTAB. Samples HTAB1, N4 and SDS4 have additional wurtzite-type ZnO phase [24] impurities, while samples N2 and HTAB2, where $ZnCl_2$ and $CS(NH_2)_2$ were used as starting materials, additionally contain the ZnS hexagonal phase [24]. The formation of particles with the smallest crystallite size of 3.4(2) nm occurs when the SDS surfactant is used (Table 2). Regardless of the used surfactant, nanopowders with small crystallite sizes (below 7 nm) are produced when $Zn(CH_3COO)_2 \cdot 2H_2O$ or $CS(NH_2)_2$ were used.

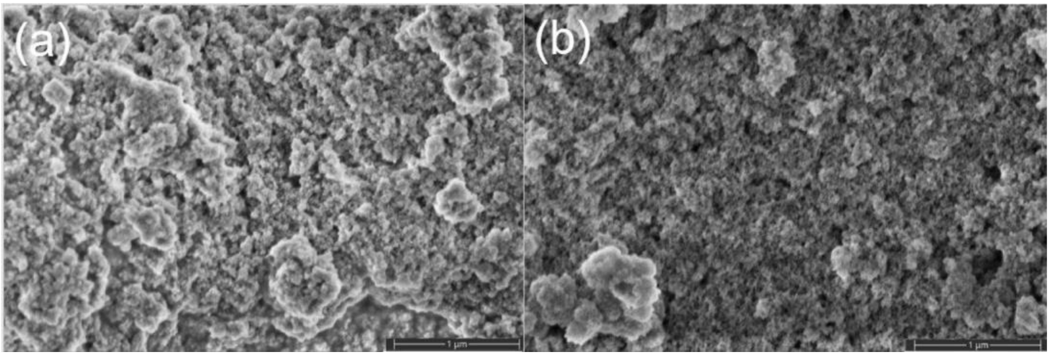

Fig. 2. SEM images of nanoparticles in the samples (a) N3 and (b) HTAB3.

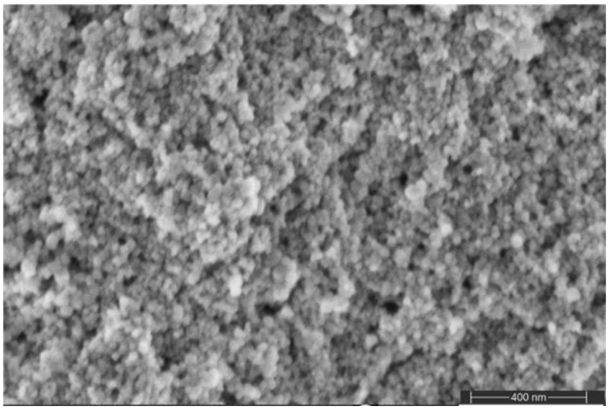

Fig. 3. SEM image of nanoparticles in the sample SDS1.

Rietveld refinement was used to determine the values of the lattice constant *a* (for the ZnS cubic phase) and the average size of the crystallites *D* from the X-ray diffraction patterns (Table 2). The lattice constant was found to be in the range of 5.400(2)–5.410(2) Å, which is close to the zinc blende value of $a = 5.410$ Å [25].

3.2. SEM

The SEM images demonstrate the formation of aggregates (10 µm) of small particles with sizes below 200 nm for samples N1, N3, HTAB1, HTAB3 and SDS1 (Figs. 2 and 3). Since $ZnCl_2$ was used as a starting material for the synthesis of these samples, it can be concluded that $ZnCl_2$ contributes to the formation of nanoparticle aggregates, which was previously observed in other studies [20,26,27].

Additionally, some of the samples contain spherical particles with a size of a few micrometers (0.2-25 µm). Spherical particles formed from smaller particles (about 1 µm) during the growth process are observed in the samples HTAB4, SDS2, and SDS4 (Fig. 4). Previously, Yao et al. [28] reported that the sphalerite ZnS spheres assemble in tight structures on high-temperature surfaces and spots [12].

In the samples SDS2, SDS3 and SDS4, 0.5-10 µm cauliflower-like particles can also be seen (Fig. 5). This means that SDS as a surfactant does not cause the agglomeration of particles. As follows, the particles undergo Ostwald ripening and an oriented attachment took place during the synthesis [29].

The most diverse formation of flower-like structures is observed for the samples N2, N4, HTAB2, HTAB4 and SDS4 (Figs. 6 and 7). It is thought that the $Zn(CH_3COO)_2{\cdot}2H_2O$ zinc source is responsible for the formation and growth of this type of structure. The growth mechanism was proposed by Ebrahimi et al. [30]. Multiple particles self-aggregate into nanoflakes to minimize the surface energy. The growth of the resulting nanoflakes is managed by a dissolution and recrystallization process. By changing the synthesis parameters, for instance, the reaction time or concentration of the used surfactant, the size of the formed structures can be controlled. From all the samples, where $Zn(CH_3COO_2{\cdot}2H_2O$ was used as Zn precursor, the formation of this type of structure

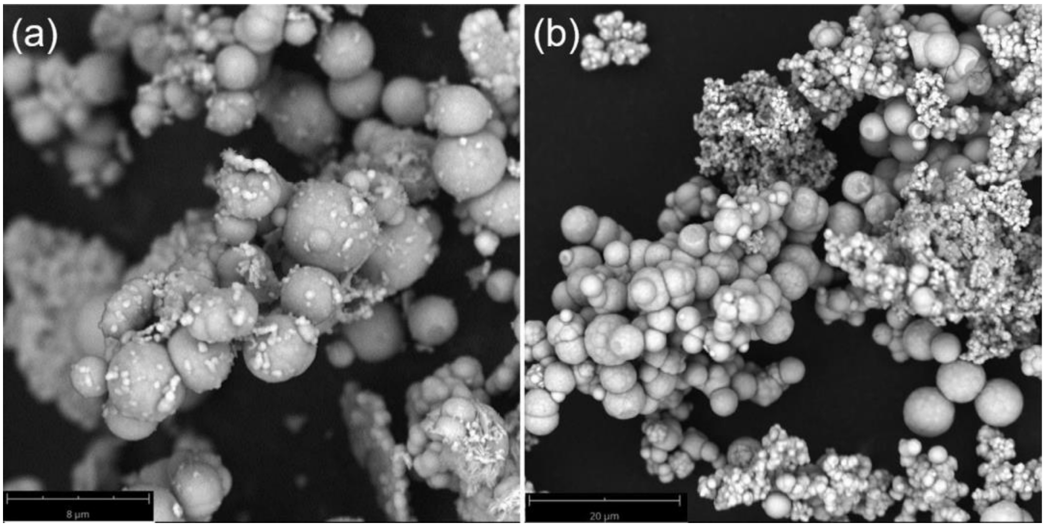

Fig. 4. SEM images of spherical particles in the samples (a) HTAB4 and (b) SDS4.

has not been detected for SDS2, but the size of these structures is smaller for the sample SDS4 than for the other samples (1-5 µm) (Fig. 7). Therefore, it can be hypothesized that SDS acts as an inhibitor for 1D crystallite growth or suppresses the formation of flower-like structures.

For the sample N4, clusters of rod-shaped agglomerates (Fig. 8) have been found. This type of structure could be formed as the result of successive stages of self-aggregation, oriented attachment and Ostwald ripening stages [30].

To gain further insight into the formation of particles and their structure, a particle of the sample SDS4 was dissected by using FIB. It can be seen (Fig. 9) that the structure inside the particle is solid, containing only small pores. This suggests that the particle formation process is overall stable and the flower- like structures are not caused by surface tension disbalance, but start to form early on in the synthesis process and continue their growth through the process.

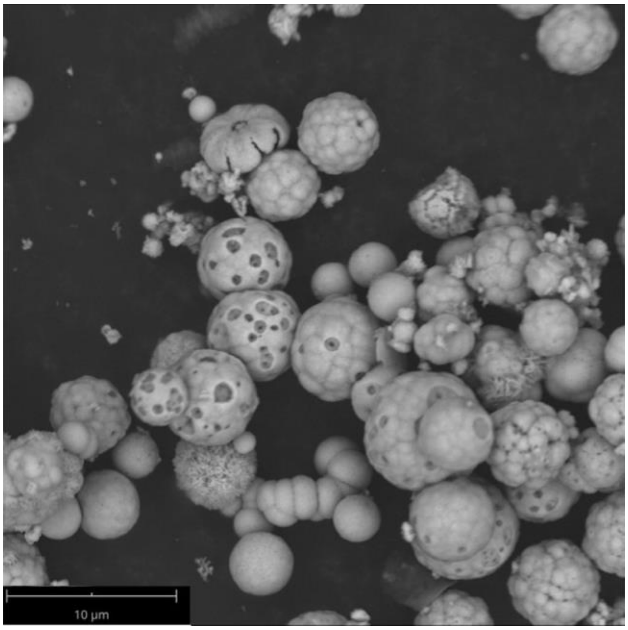

Fig. 5. SEM image of spherical particles with a highly rough surface in the sample SDS4.

Table 3
Elemental composition determined from EDX data.

Sample	Zn, at%	S, at%	Cu, at%
N1	51 ± 7	49 ± 7	0.70 ± 0.10
HTAB1	55 ± 33	45 ± 32	0.80 ± 0.60
SDS1	48 ± 4	51 ± 4	0.63 ± 0.14
N2	53 ± 10	44 ± 11	3.50 ± 1.00
HTAB2	48 ± 14	48 ± 13	4.50 ± 1.60
SDS2	59 ± 7	41 ± 7	0.83 ± 0.14
N3	50 ± 1	49 ± 2	0.80 ± 0.30
HTAB3	52 ± 27	46 ± 29	1.20 ± 1.30
SDS3	48 ± 4	51 ± 3	0.70 ± 0.40
N4	51 ± 7	48 ± 6	1.00 ± 2.00
HTAB4	53 ± 11	46 ± 12	1.30 ± 1.00
SDS4	55 ± 23	43 ± 23	1.50 ± 0.90

3.3. *EDX*

EDX data (Table 3) confirm that the ratio of Zn to S is close to 1:1 for all the samples. Samples HTAB2, SDS1 and SDS3 have a higher S content than that for Zn, while all other samples have the highest Zn content of all elements (seen also as S_i interstitials in the photoluminescence data below). Among all the samples obtained by the hydrothermal synthesis without adding any surfactants and with the addition of HTAB, the highest copper concentration was found in sample N2 (3.5 ± 1.0 at.%) and sample HTAB2 (4.5 ± 1.6 at.%), where both ZnCl$_2$ and CS(NH$_2$)$_2$ were used as starting materials. In all four cases, it was found that the addition of HTAB contributes to an increase in the concentration of Cu. This allows us to assume that the type of surfactant used for the synthesis plays a vital role in the resulting Cu concentration. Regardless of the addition of surfactants, the lowest copper content was determined in systems N1 (0.70 ± 0.10 at.%), HTAB1 (0.8 ± 0.6 at.%) and SDS1 (0.63 ± 0.14 at.%), where ZnCl$_2$ and Na$_2$S 9H$_2$O were used as starting materials. For the series of samples where SDS was added, the Cu concentration in all the samples is close and does not exceed 1.5 at.%.

3.4. *Photoluminescence*

The dependence of the integrated photoluminescence intensity on the method of synthesis and the copper concentration, as determined by EDX measurements, is shown in Fig. 10. Over- all the highest luminescence intensity was seen for samples in

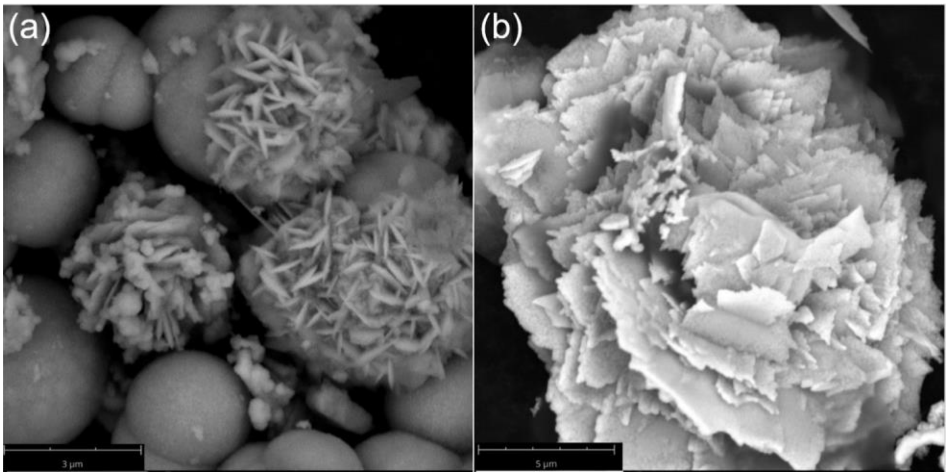

Fig. 6. SEM image of flower-like structures in the samples (a) N4 and (b) HTAB2.

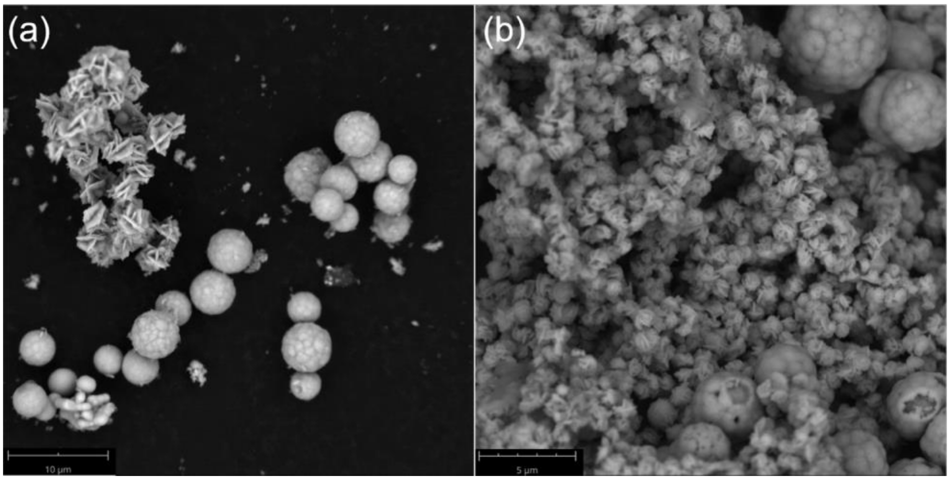

Fig. 7. SEM image of flower-like structures in the samples (a) HTAB4 and (b) SDS4.

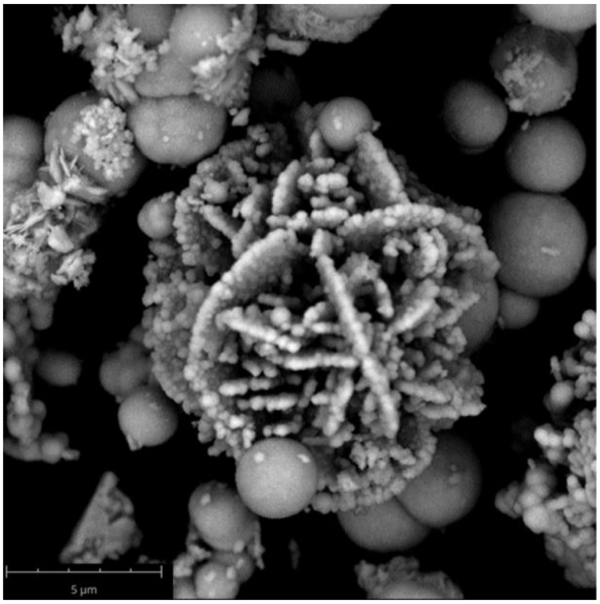

Fig. 8. SEM image of a cluster of rod-shaped agglomerates in the sample N4.

group 4, which were synthesized using the $Zn(CH_3COO)_2 \cdot 2H_2O$ zinc precursor and $CS(NH_2)_2$ sulfur precursor, with N4 showing the most intense luminescence and HTAB4 and SDS4 having high intensities as well. Sample SDS2 also showed a high luminescence intensity, however, the luminescence from samples N2 and HTAB2 was significantly less intense, possibly due to concentration quenching at higher Cu at% values.

Deconvolution of the photoluminescence spectra into Gaussian bands was performed and is shown in Fig. 11. Samples in group 4, which showed the highest luminescence intensity, also demonstrate photoluminescence spectra consisting of fewer underlying bands than the rest of the samples. The PL spectra of samples N4 and HTAB4 consist of a single band at 2.08 and 2.12 eV, respectively, and the PL spectrum of SDS4 has two bands at 2.10 and 2.75 eV (Fig. 11(d)).

In a study by Curcio et al. [31], five mechanisms of photoluminescence emission in ZnS:Cu were proposed and are as follows:

(1) 2.00 eV – $Cu^{4}T_1$ level to the $^{6}A_1$ level;
(2) 2.13 eV – ZnS conduction band to Zn vacancy;

Table 4
Position (in eV) of the bands obtained by Gaussian deconvolution.

	Cu	VZn	V_s	Zn_i	S_i	S_x/Zn_x
N1			2.33		2.85	
HTAB1	2.1			2.62	2.78	3.35
SDS1		2.22			2.83	3.3
N2			2.3		2.85	3.3
HTAB2		2.19			2.8	3.24
SDS2	2.09			2.57	2.85	
N3		2.2			2.73	3.25
HTAB3		2.18			2.78	3.3
SDS3			2.33		2.85	
N4	2.08					
HTAB4	2.1				2.75	
SDS4	2.12					

(3) 2.37 eV – sulfur vacancy to ZnS valence band;
(4) 2.59 eV – zinc interstitial to ZnS valence band;
(5) 2.83 eV – ZnS conduction band to sulfur interstitial.

In our study, we found that the Gaussian deconvolution bands can be grouped into six non-overlapping ranges with the emission energies of (1) 2.08–2.12 eV, (2) 2.18–2.22 eV, (3) 2.30–2.33 eV, (4) 2.57–2.62 eV, (5) 2.73–2.85 eV and (6) 3.24–3.35 eV, as shown in Table 4.

A significant difference of around 0.1 eV can be seen between the proposed energies by Curcio et al. and our results in the first group, where we assume the emission occurs in Cu ions due to the transition $^{4}T_1 \rightarrow {}^{6}A_1$. Here we reason that since samples N4 and HTAB4 demonstrate only one Gaussian band and have the highest integrated luminescence intensities (an indication that there are few intrinsic defects in the ZnS:Cu structure), the observed luminescence arises due to the transition $^{4}T_1 \rightarrow {}^{6}A_1$ rather than $ZnS_{CB} \rightarrow V_{Zn}$. Additionally, due to a mixture of cubic and hexagonal phases, an increase of the band gap from 3.68 eV in the cubic phase to 3.77 eV in the hexagonal phase is possible [32].

An additional band located at 3.24–3.35 eV (Table 4) is observed for samples in the first three groups. It is suggested that its cause is the trapping and recombination of electrons with holes due to sulfur or zinc defect states [33–35].

The obtained data show that the most abundant defect is the interstitial sulfur defect S_i. The origin of this defect is explained as being due to the larger ionic size of sulfur ions (1.7 Å) compared to zinc ions (0.74 Å), causing more strain in the ZnS lattice, which leads to lower binding energy in the electron levels produced by interstitial sulfur [36].

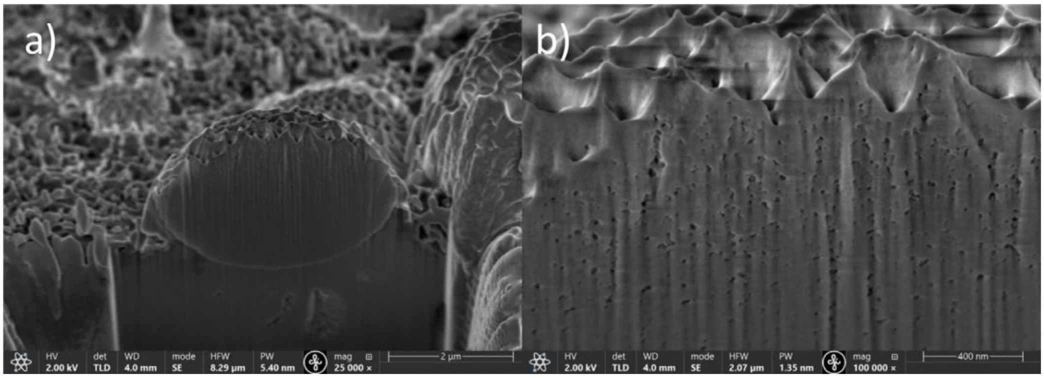

Fig. 9. SEM image of a dissected particle in the sample SDS4.

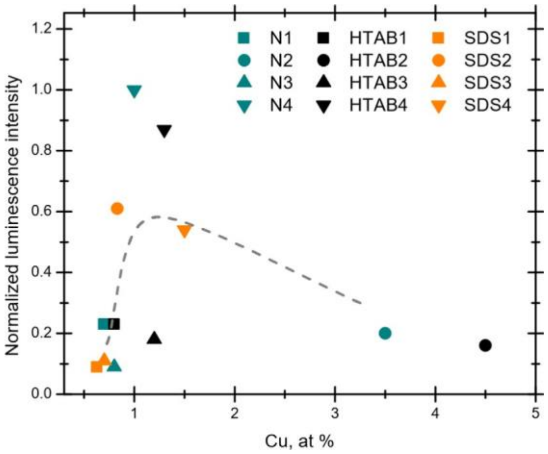

Fig. 10. Dependence of the integrated photoluminescence intensity on the method of synthesis and Cu concentration.

The overall luminescence is more intense in samples containing larger particles. Indeed, the samples SDS2, N4, HTAB4 and SDS4, having micrometer sized particles, demonstrate the strongest luminescence. This means that surface defects play a significant role in the luminescence properties and the luminescence is stronger when the volume-to-surface ratio of particles increases. The high luminescence output of these samples also suggests that the surfactant affects the photoluminescence intensity and spectrum less than the zinc and sulfur precursor choice. However, the rest of the defects, such as V_{Zn}, V_s, and Zn_i, offer no clear correlation and might be the result of a complex interaction between the chosen precursors and surfactants.

The CIE 1931 color space diagram is shown in Fig. 12. It can be seen that samples N4, HTAB4 and SDS4 lean into the orange end (d-d transitions in Cu ions) of the diagram, as is expected by their single (and double for HTAB4) Gaussian bands at 2.08, 2.10 and 2.12 eV (2.75 eV). Samples SDS1 and SDS3 visually show a slightly green emission that is more indicative of intrinsic defects in the structure rather than Cu photoluminescence.

3.5. Translucency

All the samples were pressed into ceramic pellets with a diameter of 5 mm and a thickness of 0.2 mm. Samples N3 and HTAB3 showed visible translucency, as shown in Fig. 13. Sample SDS3 also showed an inclination to translucency, however it was too dark to transmit light under normal conditions. The rest of the samples were completely opaque. This can be explained by SEM images showing that samples N3 and HTAB3 consist of nanoparticles as opposed to microparticles seen in the other samples, and samples N3, HTAB3 and SDS3 being of the pure cubic phase. Chen et al. have demonstrated that the hexagonal phase decreases the optical transparency by causing birefringence [7].

3.6. EXAFS

EXAFS spectra were measured for the SDS sample series. Very similar spectra were obtained for samples SDS1 and SDS3, and samples SDS2 and SDS4. Although the SDS4 sample has a higher PL intensity than SDS2, it also shows an additional ZnO phase revealed in the XRD data. Therefore, SDS2 and SDS3 samples were selected and analyzed in detail. The results of the RMC simulations of the Zn and Cu K-edge EXAFS spectra $\chi(k)k^2$ of SDS2 and SDS3 samples measured at 10 K are shown in Fig. 14. Good agreement between the experimental and calculated spectra is observed in the k and R spaces as well as in the WT(k,R)-space within one structural model with the zinc blende ZnS crystallographic structure [21] and lattice parameters obtained by XRD. The obtained result suggests that copper atoms substitute zinc, nevertheless, the substitution is accompanied by local distortions. Two differences are well visible. Firstly, the amplitude of the EXAFS oscillations at the Zn K-edge is larger for the SDS3 sample than for the SDS2 sample. Also, the amplitude of peaks in the Fourier transform of the EXAFS spectrum is significantly larger for the SDS3 sample, especially for outer coordination shells located at long distances. This result correlates well with a larger size of the crystallites in the SDS3 sample compared to that in the SDS2 sample (Table 2). Secondly, the EXAFS oscillations at the Cu K-edge are rather close in both samples and differ from that at the Zn K-edge suggesting the presence of a disordered environment around the copper atoms. In fact, the second peak in the FTs at about 3–4 Å has a smaller amplitude at the Cu K-edge.

More quantitative structural information on the short-range order around the Zn and Cu atoms was obtained from the analysis of the atomic coordinates in the RMC simulation box. The partial radial distribution functions (RDFs) $g(R)$ were calculated for the first three coordination shells of the metal atoms and these are shown in Fig. 15. The values of the mean-square displacements (MSDs) for the Zn, S and Cu atoms, and the mean-square relative displacements (MSRDs) for Zn–S, Zn–Zn, Cu–S and Cu–Zn atom pairs were also evaluated and are reported in Table 5.

Several conclusions can be drawn from the analysis of the RDF shapes. The RDFs for Zn–S_1, Zn–Zn_2 and Zn–S_3 atom pairs corresponding to the first three coordination shells of zinc have narrower peaks for the SDS3 sample, which has larger sizes of the crystallites (Table 2). The peak broadening in the SDS2 sample, having about four times smaller sizes of the crystallites, is related to the structural relaxation of a large number of atoms located

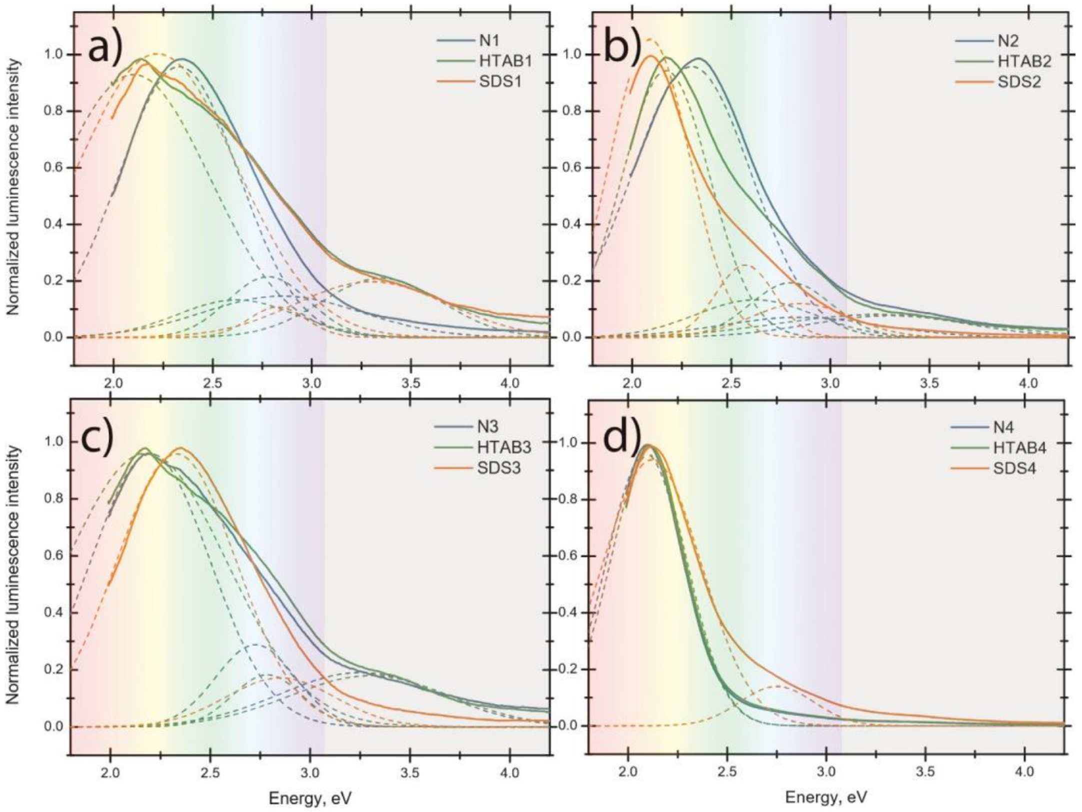

Fig. 11. Gauss deconvolution of the PL spectra.

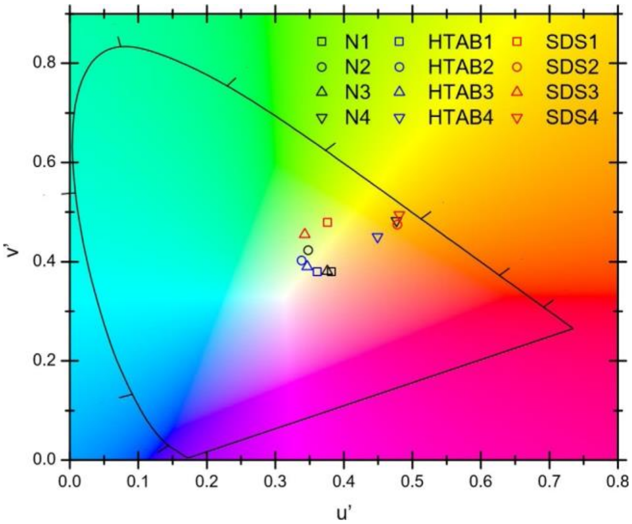

Fig. 12. CIE 1931 color space diagram.

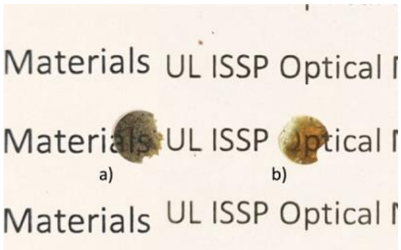

Fig. 13. Pressed ceramic samples (a) HTAB3 and (b) N3.

Table 5
The mean-square displacements (MSDs) for Zn, S and Cu atoms, and the mean square relative displacements (MSRDs) for Zn–S, Zn–Zn, Cu–S and Cu–Zn atom pairs in SDS2 and SDS3 ZnS:Cu samples obtained from the RMC simulations. The coordination shell number is indicated as a subscript. Values of MSD and MSRD are in Å^2.

	SDS2	SDS3
MSD(Zn)	0.15	0.09
MSD(Cu)	0.22	0.24
MSD(S)	0.15	0.11
MSRD(Zn–S_1)	0.009	0.005
MSRD(Cu–S_1)	0.010	0.008
MSRD(Zn–Zn_2)	0.020	0.006
MSRD(Cu–Zn_2)	0.039	0.031
MSRD(Zn–S_3)	0.020	0.008
MSRD(Cu–S_3)	0.028	0.031

at the surface of the nanoparticles or near it, that leads to an increase in static disorder. At the same time, the broadening of RDFs for the Cu–S and Cu–Zn atom pairs is comparable in both samples, indicating similarities of the short-range order around impurity copper ions. Notably, the local environment of the copper ions is more distorted than that of zinc, especially in the SDS3 sample. More quantitatively, the observed disorder effects can be described in terms of the MSD and MSRD factors (Table 5). The value of the MSD for Cu is 1.5 (2.5) times larger than for Zn in the SDS2 (SDS3) sample. This fact is indicative of local disorder induced by the substitution, leading to the wider distribution of interatomic distances reflected by the MSRD values.

Finally, the relaxation of the local environment around the Cu ions results in different interatomic bond lengths in the first coordination shell of the metal cations. In both samples, the interatomic distances are equal to $R(\text{Cu}–S_1)$ = 2.25(2) Å and $R(\text{Zn}–S_1)$ = 2.33(2) Å. This difference (0.08 Å) is somewhat larger than

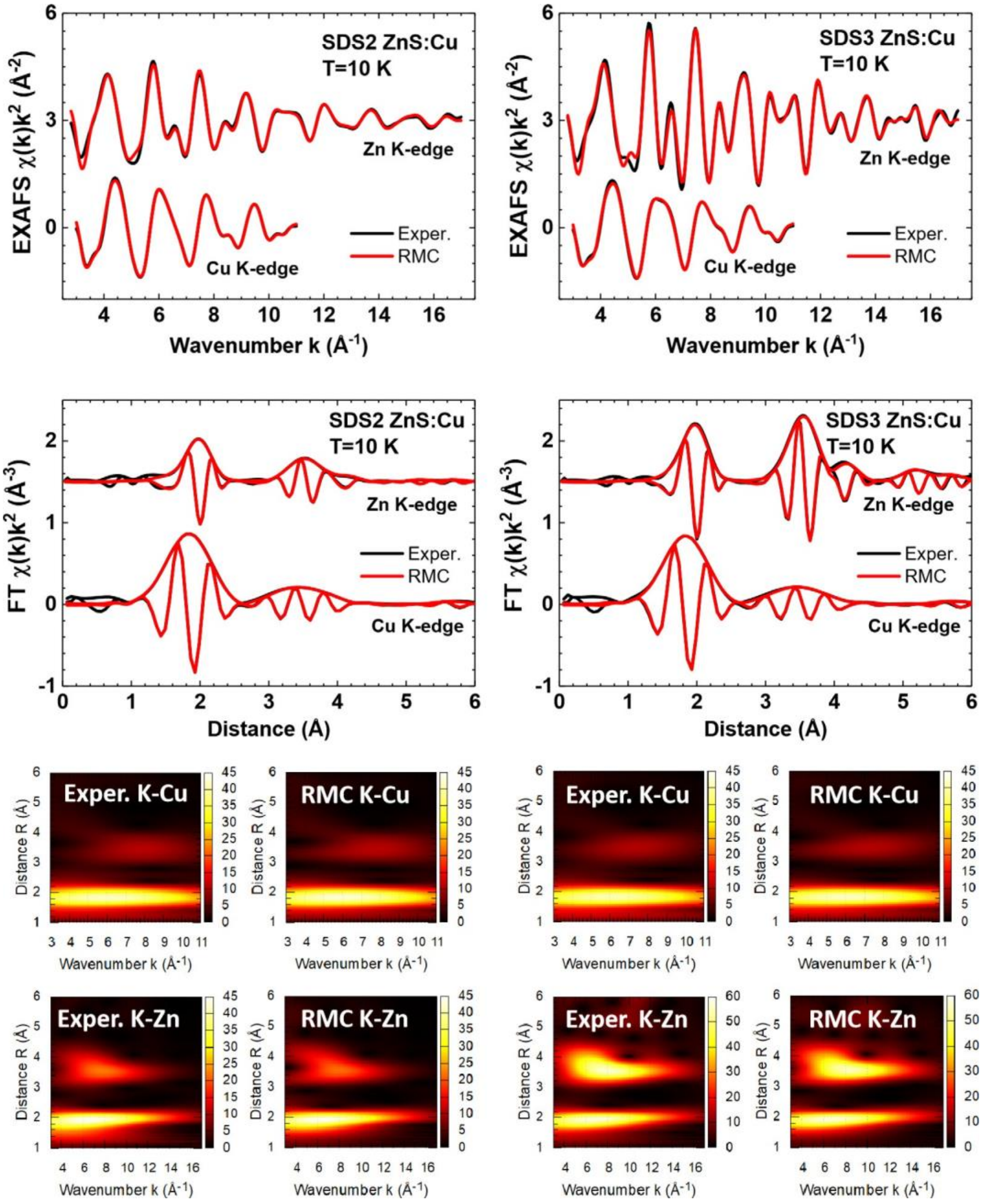

Fig. 14. Experimental and RMC-calculated Zn and Cu K-edges EXAFS spectra $\chi(k)k^2$ and their Fourier and Morlet wavelet transforms (FTs and WTs) for SDS2 and SDS3 ZnS:Cu samples at $T = 10$ K. Note that the peaks in FTs and WTs are located at distances that are slightly shorter than their crystallographic values because both transforms were not corrected for the phase shift present in the EXAFS equation.

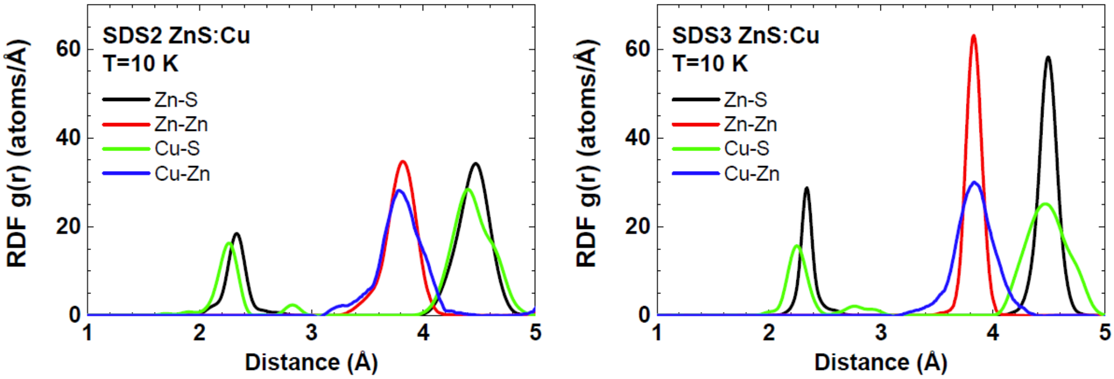

Fig. 15. Radial distribution functions (RDFs) $g(r)$ for Zn–S, Zn–Zn, Cu–S and Cu–Zn atom pairs in SDS2 and SDS3 ZnS:Cu samples at $T = 10$ K.

the one expected from the difference in the ionic radii (0.03 Å) for the four-fold coordinated cations, *r* (Cu^{2+}) = 0.57 Å and r(Zn^{2+}) = 0.60 Å. Note that the difference in the positions of the second and third coordination shells of the Cu and Zn ions is negligible.

4. Conclusions

ZnS:Cu samples were synthesized using the hydrothermal method from $ZnCl_2$ and $Zn(CH_3COO)_2 \cdot 2H_2O$ zinc precursors in combination with $CS(NH_2)_2$ and $Na_2S \cdot 9H_2O$ sulfur precursors. Additionally, the samples were also prepared with and without surfactant, SDS or HTAB.

XRD data show that the cubic zinc blende phase is prevalent in most samples, except in samples N2, HTAB2 and SDS2. Samples N3, HTAB3 and SDS3 contained only the cubic phase. Moreover, the analysis of SEM images indicates that samples N3 and HTAB3 consist of nanoparticles. Overall, it was seen that the hexagonal phase decreases translucency and the most translucent samples were of 100% cubic phase, as was expected according to the literature. However, the phase is not the only determinant of the resulting optical properties and the morphology of the samples plays an equally significant role in the production of translucent ceramics.

SEM images of a particle dissection in sample SDS4 show that the internal structure of the spherical particles is solid with small pores. This suggests that the particle formation process is stable.

Photoluminescence spectra were deconvoluted into a set of Gaussian bands, whose origin was interpreted based on published data. It was found that intrinsic defects were abundant in all samples except for N4 and SDS4, in which only a single band for the transition $^4T_1 \rightarrow {}^6A_1$ in Cu ions was seen. The overall luminescence was higher for samples containing larger particles, with the presence of micrometer-ranged particles in SDS2, N4, HTAB4 and SDS4 leading to a high luminescence intensity as compared to the rest of the samples. This means that a significant amount of defects is located at the surface of particles, leading to luminescence quenching in particles with higher surface-to-volume ratios.

The local atomic structure of ZnS:Cu nanoparticles (samples SDS2 and SDS3) was studied by X-ray absorption spectroscopy at the Zn and Cu K edges. Analysis of the Zn and Cu K-edge EXAFS spectra recorded at 10 K using the reverse Monte Carlo method confirmed that copper ions substitute zinc ions in the cubic zinc blende structure. The difference in ion sizes is responsible for the shorter interatomic distances Cu–S (2.25(2) Å) compared to Zn–S (2.33(2) Å). The local structure relaxation around the metal cations is larger in smaller nanocrystallites and is responsible for the large values of the MSD factors for Zn and Cu atoms, calculated relative to the ideal positions of atoms in the zinc blende structure. The short-range order around the copper ions is distorted compared to that around zinc ions, which results in a wider distribution of Cu–S distances as reflected by the large values of the MSRD factors.

In conclusion, the addition of a surfactant or choice of precursors allows for control of the morphology and optical properties of ZnS:Cu nanopowders, which can potentially impact their use in electroluminescent devices.

CRediT authorship contribution statement

Milena Dile: Investigation, Conceptualization, Validation, Writing – original draft, Writing – review & editing. **Katrina Laganovska:** Investigation, Conceptualization, Validation,

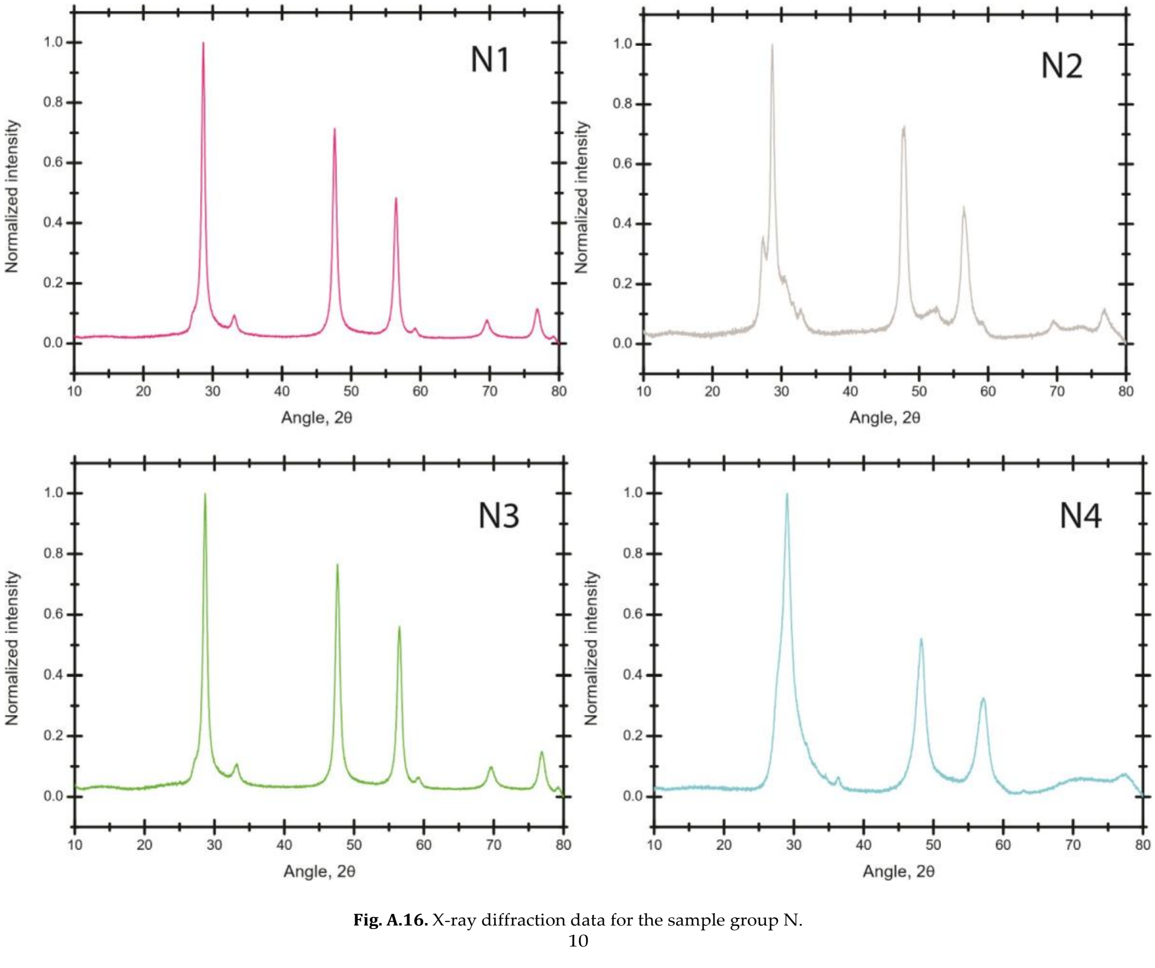

Fig. A.16. X-ray diffraction data for the sample group N.

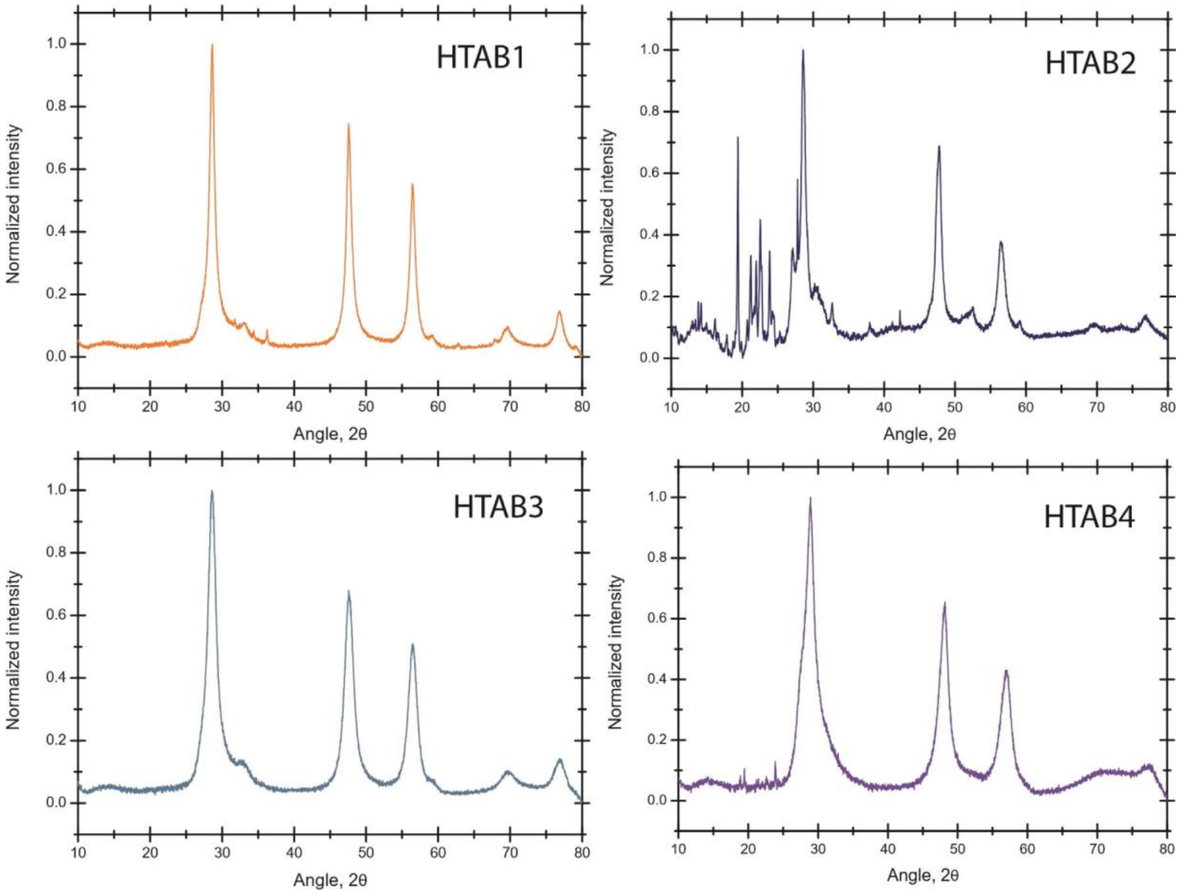

Fig. A.17. X-ray diffraction data for the sample group HTAB.

Writing – original draft, Writing – review & editing. **Aleksejs Zolotarjovs:** Investigation, Conceptualization, Resources, Writing – original draft, review & editing, Supervision. **Ivita Bite:** Investigation, Review & editing. **Edgars Vanags:** Investigation. **Inga Pudza:** Investigation, Writing – original draft, Writing – review & editing. **Alexei Kuzmin:** Investigation, Conceptualization, Validation, Formal analysis, Writing – original draft, Writing – review & editing. **Krisjanis Smits:** Investigation, Resources, Funding acquisition.

Declaration of competing interest

The authors declare that they have no known competing financial interests or personal relationships that could have appeared to influence the work reported in this paper.

Data availability

Data will be made available on request.

Acknowledgments

The financial support of the ERDF project No. 1.1.1.1/21/A/055 is greatly acknowledged. We acknowledge DESY (Hamburg, Germany), a member of the Helmholtz Association HGF, for the provision of experimental facilities. Parts of this research were carried out at PETRA III and we would like to thank Dr. Edmund Welter for his assistance in using the P65 beamline. Beamtime was allocated for proposal I-20220381 EC. The Institute of Solid State Physics, University of Latvia as the Center of Excellence has received funding from the European Union's Horizon 2020 Framework Programme H2020-WIDESPREA-D-01-2016-2017-TeamingPhase2 under grant agreement No. 739508, project CAMART2.

Appendix. XRD data

See Figs. A.16–A.18.

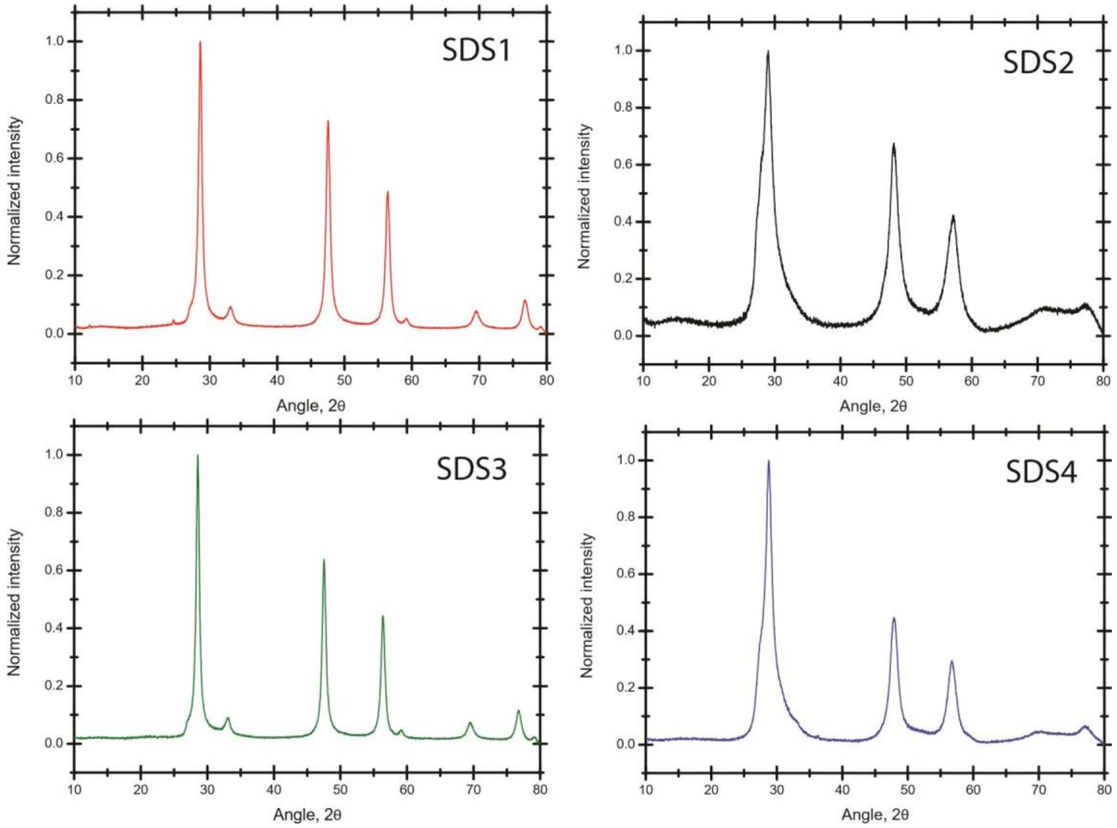

Fig. A.18. X-ray diffraction data for the sample group SDS.

References

[1] R. Hernández Castillo, M. Acosta, I. Riech, G. Santana-Rodríguez, J. Mendez-Gamboa, C. Acosta, M. Zambrano, Study of ZnS/CdS structures for solar cells applications, Optik 148 (2017) 95–100, http://dx.doi.org/10.1016/j.ijleo.2017.09.002.

[2] L. Mandal, Vidya, B. Verma, J. Rani, P.K. Patel, Progressive advancement of ZnS-based quantum dot LED, Opt. Quantum Electron. 53 (2021) 10, http://dx.doi.org/10.1007/s11082-020-02653-6.

[3] S. Tarish, Y. Xu, Z. Wang, F. Mate, A. Al-Haddad, W. Wang, Y. Lei, Highly efficient biosensors by using well-ordered ZnO/ZnS core/shell nanotube arrays, Nanotechnology 28 (2017) 405501, http://dx.doi.org/10.1088/13616528/aa82b0.

[4] A. Tiwari, S.J. Dhoble, Critical analysis of phase evolution, morphological control, growth mechanism and photophysical applications of ZnS nanostructures (zero-dimensional to three-dimensional): A review, Cryst. Growth Des. 17 (2017) 381–407, http://dx.doi.org/10.1021/acs.cgd. 6b01463.

[5] M. Bredol, H. Schulze Dieckhoff, Materials for powder based AC-electroluminescence, Materials 3 (2010) 1353–1374, http://dx.doi.org/10.3390/ma3021353.

[6] C. Chlique, O. Merdrignac-Conanec, N. Hakmeh, X. Zhang, J.L. Adam, Transparent ZnS ceramics by sintering of high purity monodisperse nanopowders, J. Am. Ceram. Soc. 96 (2013) 3070–3074, http://dx.doi.org/10.1111/jace.12570.

[7] Y. Chen, L. Zhang, J. Zhang, P. Liu, T. Zhou, H. Zhang, D. Gong, D. Tang, D. Shen, Fabrication of transparent ZnS ceramic by optimizing the heating rate in spark plasma sintering process, Opt. Mater. 50 (2015) 36–39, http://dx.doi.org/10.1016/j.optmat.2015.03.058.

[8] A. Klausch, H. Althues, C. Schrage, P. Simon, A. Szatkowski, M. Bredol, D. Adam, S. Kaskel, Preparation of luminescent ZnS:Cu nanoparticles for the functionalization of transparent acrylate polymers, J. Lumin. 130 (2010) 692–697, http://dx.doi.org/10.1016/j.jlumin.2009.11.021.

[9] G.R. Durand, N. Hakmeh, V. Dorcet, V. Demange, F. Cheviré, O. Merdrignac-Conanec, New insights in structural characterization of transparent ZnS ceramics hot-pressed from nanocrystalline powders synthesized by combustion method, J. Eur. Ceram. Soc. 39 (2019) 3094–3102, http://dx.doi.org/10.1016/j.jeurceramsoc.2019.03.033.

[10] X. Liu, X. Cai, J. Mao, C. Jin, ZnS/Ag/ZnS nano-multilayer films for transparent electrodes in flat display application, Appl. Surf. Sci. 183 (2001) 103–110, http://dx.doi.org/10.1016/S0169-4332(01)00570-0.

[11] R. Krsmanovi, E. Salernitano, S. Grilli, G. Magnani, F. Mazzanti, L. Pilloni, A. Montone, ZnS wurtzite ceramic fabrication by a simple and cost effective pressureless sintering method: A microstructure development overview, Microscopie 31 (2020) http://dx.doi.org/10.4081/microscopie.2020.9203.

[12] L. Zhang, L. Yang, Hydrothermal growth of ZnS microspheres and their temperature-dependent luminescence properties, Cryst. Res. Technol. 43 (2008) 1022–1025, http://dx.doi.org/10.1002/crat.200800092.

[13] N. Doebelin, R. Kleeberg, Profex: a graphical user interface for the rietveld refinement program BGMN, J. Appl. Crystallogr. 48 (2015) 1573–1580, http://dx.doi.org/10.1107/S1600576715014685.

[14] E. Welter, R. Chernikov, M. Herrmann, R. Nemausat, A beamline for bulk sample x-ray absorption spectroscopy at the high brilliance storage ring PETRA III, in: AIP Conf. Proc., Vol. 2054, 2019, 040002, http://dx.doi.org/10.1063/1.5084603.

[15] A. Kalinko, Xaesa v0.06, 2022, URL https://github.com/aklnk/xaesa.

[16] A. Kuzmin, J. Chaboy, EXAFS and XANES analysis of oxides at the nanoscale, IUCrJ 1 (2014) 571–589, http://dx.doi.org/10.1107/S2052252514021101.

[17] J. Timoshenko, A. Kuzmin, J. Purans, Reverse monte carlo modeling of thermal disorder in crystalline materials from EXAFS spectra, Comput. Phys. Comm. 183 (2012) 1237–1245, http://dx.doi.org/10.1016/j.cpc.2012. 02.002.

[18] J. Timoshenko, A. Kuzmin, J. Purans, EXAFS study of hydrogen intercalation into ReO$_3$ using the evolutionary algorithm, J. Phys.: Condens. Matter 26 (2014) 055401, http://dx.doi.org/10.1088/09538984/26/5/055401.

[19] J. Timoshenko, A. Kuzmin, Wavelet data analysis of EXAFS spectra, Comput. Phys. Comm. 180 (2009) 920–925, http://dx.doi.org/10.1016/j.cpc.2008.12. 020.

[20] A. Kuzmin, M. Dile, K. Laganovska, A. Zolotarjovs, Microwave assisted synthesis and characterization of undoped and manganese doped zinc sulfide nanoparticles, Mater. Chem. Phys. 290 (2022) 126583, http://dx.doi.org/10.1016/j.matchemphys.2022.126583.

[21] E.A. Jumpertz, Über die elektronendichteverteilung in der zinkblende, Ber. Bunsenges. Phys. Chem. 59 (1955) 419–425, http://dx.doi.org/10.1002/bbpc.19550590520.

[22] A.L. Ankudinov, B. Ravel, J.J. Rehr, S.D. Conradson, Realspace multiple-scattering calculation and interpretation of X-ray absorption near-edge structure, Phys. Rev. B 58 (1998) 7565–7576, http://dx.doi.org/10.1103/physrevb.58.7565.

[23] J.J. Rehr, R.C. Albers, Theoretical approaches to X-ray absorption fine structure, Rev. Modern Phys. 72 (2000) 621–654, http://dx.doi.org/10.1103/revmodphys.72.621.

[24] E.H. Kisi, M.M. Elcombe, U parameters for the wurtzite structure of ZnS and ZnO using powder neutron diffraction, Acta Crystallogr. C 45 (1989) 1867–1870, http://dx.doi.org/10.1107/S0108270189004269.

[25] J.C. Jamieson, H.H. Demarest, A note on the compression of cubic ZnS, J. Phys. Chem. Solids 41 (1980) 963–964, http://dx.doi.org/10.1016/00223697(80)90101-8.

[26] M. Xin, L.-M. Liao, F. Han, Optical properties of ZnS: Ce nanocrystals prepared by hydrothermal method, J. Lumin. 238 (2021) 118074, http://dx.doi.org/10.1016/j.jlumin.2021.118074.

[27] X. Mei, H. Li-Zhong, Luminescence properties of ZnS:Cu, Eu semiconductor nanocrystals synthesized by a hydrothermal process, Chin. Phys. B 22 (2013) 087804, http://dx.doi.org/10.1088/1674-1056/22/8/087804.

[28] Q.-Z. Yao, G. Jin, G.-T. Zhou, Formation of hierarchical nanospheres of ZnS induced by microwave irradiation: A highlighted assembly mecha- nism, Mater. Chem. Phys. 109 (2008) 164–168, http://dx.doi.org/10.1016/j.matchemphys.2007.11.010.

[29] Y. Kim, D. Amaranatha Reddy, H. Park, T.K. Kim, Anionic precursor-mediated morphology-controlled synthesis of ZnS nanostructures: Morphology-dependent tunable photoluminescence in the visible region and pulsed laser-induced efficient reduction of Cr(VI), Ceram. Int. 42 (2016) 12046–12054, http://dx.doi.org/10.1016/j.ceramint.2016.04.132.

[30] S. Ebrahimi, B. Yarmand, Morphology engineering and growth mechanism of ZnS nanostructures synthesized by solvothermal process, J. Nanopart. Res. 21 (2019) 264, http://dx.doi.org/10.1007/s11051-019-4714.

[31] A.L. Curcio, L.F. da Silva, M.I.B. Bernardi, E. Longo, A. Mesquita, Nanostructured ZnS:Cu phosphor: Correlation between photoluminescence properties and local structure, J. Lumin. 206 (2019) 292–297, http://dx.doi.org/10.1016/j.jlumin.2018.10.073.

[32] A.K. Kole, P. Kumbhakar, Cubic-to-hexagonal phase transition and optical properties of chemically synthesized ZnS nanocrystals, Results Phys. 2 (2012) 150–155, http://dx.doi.org/10.1016/j.rinp.2012.09.010.

[33] D. Saikia, J.P. Borah, M. Jangra, A. Puzari, Investigation of photophysical properties of ZnS:Mn^{2+}nanoparticles, Indian J. Phys. 90 (2016) 549–555, http://dx.doi.org/10.1007/s12648-015-0780-y.

[34] P. Kumari, A. Sharma, A. Kumawat, S. Samanta, K.P. Misra, A. Rao, S. Kabi, S. Chattopadhyay, Strong UV emission in flakes-like ZnS nanoparticles synthesized by cost effective sol–gel method, Mater. Today Proc. 58 (2022) 642–647, http://dx.doi.org/10.1016/j.matpr.2022.01.353.

[35] Y. Liu, Z. Li, W. Zhong, L. Zhang, W. Chen, Q. Li, Synthesis and photoluminescence properties of ZnS nanobowl arrays via colloidal monolayer template, Nanoscale Res. Lett. 9 (2014) 389, http://dx.doi.org/10.1186/ 1556-276X-9389.

[36] R. Kripal, A.K. Gupta, S.K. Mishra, R.K. Srivastava, A.C. Pandey, S.G. Prakash, Photoluminescence and photoconductivity of ZnS:Mn^{2+} nanoparticles synthesized via co-precipitation method, Spectrochim. Acta A 76 (2010) 523–530, http://dx.doi.org/10.1016/j.saa.2010.04.018.